MAX-PLANCK-GESELLSCHAFT
Published in: Physical Chemistry Chemical Physics 3 (2001), 1114-1122, published 26.02.2001

Bulk and surface phases of iron oxides in oxygen and water atmosphere at low pressure

G. Ketteler, W. Weiss, W. Ranke*, R. Schlögl

Department of Inorganic Chemistry, Fritz-Haber-Institute of the MPG, Faradayweg 4-6, 14195 Berlin, Germany

* Corresponding author: e-mail ranke@fhi-berlin.mpg.de, phone +49 30 8413 4523, fax +49 30 8413 4401

Submitted 20 November 2000; accepted 19 January 2001

Abstract

Thermodynamic stability ranges of different iron oxides were calculated as a function of the ambient oxygen or water gas phase pressure ($p \leq 1$ bar) and temperature by use of the computer program EquiTherm. The phase diagram for Fe-H_2O is almost completely determined by the O_2 pressure due to the H_2O dissociation equilibrium. The formation of epitaxially grown iron oxide films on platinum and ruthenium substrates agrees very well with the calculated phase diagrams. Thin films exhibit the advantage over single crystals that bulk diffusion has only limited influence on the establishment of equilibrium phases. Near the phase boundary Fe_3O_4-Fe_2O_3, surface structures are observed consisting of biphase ordered domains of FeO(111) on both oxides. They are formed due to kinetic effects in the course of the oxidation to hematite or reduction to magnetite, respectively. Annealing a Fe_3O_4(111) film in 5×10^{-5} mbar oxygen at 920-1000K results in a new γ-Fe_2O_3(111)-like intermediate surface phase during the oxidation to α-Fe_2O_3(0001). A model is suggested for the growth of iron oxides and for redox processes involving iron oxides. The formation of several equilibrium surface phases is discussed.

1. Introduction

Iron oxides belong to frequently utilized compounds with various applications for example as high-density magnetic recording media or as pigments. In heterogenous catalysis iron oxide catalysts are used for instance in the dehydrogenation of ethylbenzene to styrene [1-3]. Heteroepitaxially grown oxide films have been found to be useful model catalyst systems for the systematic investigation of catalytic properties [3-6]. Iron oxides are furthermore of great interest with regard to corrosion and oxidation processes of iron metal and steel [7]. These processes are mediated by the surface which depends in its structure severely on environmental variables like temperature, oxygen or water partial pressures. Recently, systematic investigations of the surface structure of α-Fe_2O_3(0001) in dependence of the oxygen partial pressure were reported revealing two different surface terminations to be stable in different oxygen pressures [8]. For α-Al_2O_3(0001) and α-Fe_2O_3(0001) [9], as well as MgO(100) [10], the reaction with water vapor was studied in a pressure range from 10^{-8} torr to 10^{2} torr, and the water partial pressure for a phase transition from the clean to a hydroxilated surface was determined by synchrotron X-ray photoemission studies. The dependence of the surface structures of α-Fe_2O_3(0001) and α-Al_2O_3(0001) on the ambient oxygen pressure and water environment was subject to recent theoretical investigations [11,12].

By now, oxidation and corrosion is either studied with bulk crystals mainly by X-ray diffraction [13] or by systematic investigations of oxidized iron single crystals in ultra-high vacuum [14]. The first approach may lead to equilibrium phases but is unable to detect relevant surface phases. On the other hand, single crystals possess the drawback that the bulk crystal forms a virtually infinite reservoir of iron which can diffuse to the surface establishing for instance the often reported layer-wise formation of iron oxides on iron [7,14,15]. In case that the single-crystals are cleaned by sputter-annealing procedures, statements about thermodynamically formed surface phases become even more speculative since in most cases oxygen anions are preferentially sputtered leading to reduced surface phases, the stoichiometry of which is difficult to control reproducibly. In this paper, we show that thin oxide films can serve as excellent model systems to elucidate the thermodynamic equilibrium bulk and surface phase structures and to investigate phase transformations at elevated temperatures over an extended oxygen pressure range. This serves to systematize preparation conditions of iron oxides in ultra-high vacuum in form of surface phase diagrams which has been demanded since more than ten years [16]. We show that not only equilibrium surface phases are detected in this case but also metastable intermediate surface phases can be distinguished.

2. Calculation procedure and sample preparation

2.1 Calculation procedure

In order to calculate thermodynamic stability ranges for different iron oxide phases we made use of the commercially available program EquiTherm [17]. This program calculates

equilibrium compositions by minimizing the Gibbs energy at constant pressure (or volume) and constant temperature. The program requires as a minimum thermochemical values for the standard enthalpy of formation $\Delta H_f^0(298.15K)$, the absolute entropy of the substance (at one bar pressure and 298.15K) $S^0(298.15K)$, the heat capacity at constant pressure and temperature T $C_p(T)$, and for phase-transitions the transition temperature (at one bar pressure) and the standard enthalpy of transition (at one bar pressure at the transition temperature T_t) $\Delta H_t^0(T_t)$. These data were taken from Barin [18], where thermochemical data of more than 3100 organic and inorganic substances are stored, covering the literature up to 1988. For the participating compounds appropriate condensed and gas phases have to be defined. The specific chemical reactions are of no importance for the calculation, since the choice of different chemical substances is equivalent with the choice of a set of independent chemical reactions and only the molar amounts have to be preset. For a system of i components, the Gibbs energy can be written as

$$G = \sum_i \mu_i m_i = \sum_i (\mu_i^0 + RT \ln a_i) m_i \quad (1)$$

with μ_i^0 : chemical potential of the material in its defined standard state, m_i: mass of component i, a_i : activity with reference to this state, R: ideal gas constant, T: temperature. The masses of the various components can be systematically varied with regard to mass balance relationship:

$$\sum_i N_{ij} m_i = b_j \quad (2)$$

where N_{ij} is the number of atoms of element j in one molecule of component i with the mass m_i and b_j is the total mass for element j (with j = 1,2,3, ..., n; n is the number of components). EquiTherm makes use of a function

$$F = G + \sum_{j=1}^{m} \lambda_j \left(b_j - \sum_i N_{ij} m_i \right) \quad (3)$$

and solves it by the method of Lagrange multipliers λ_j with the secondary conditions

$$\left[\frac{\partial F}{\partial n_i} \right]_{n_{k \neq i}, \lambda} = \mu_i - \sum_j N_{ij} \lambda_j = 0 \quad (4)$$

$$= \mu_i^0 + RT \ln a_i - \sum_j N_{ij} \lambda_j = 0$$

$$\left[\frac{\partial F}{\partial \lambda_j} \right]_{\lambda_{k \neq j} n} = b_j - \sum_i N_{ij} m_i = 0 \quad (5)$$

with $m_i \geq 0$. The equilibrium system is defined by the equations (2) and (4) with the unknown variables m_i and λ_j. The logarithmic terms are linearized by developing into a first-order Taylor´s series. This results in w linear equations (w: number of molecular species). From

$$\sum_i X_i N_{ij} = \frac{b_j}{\sum_i m_i} \quad (6)$$

there occur n further equations (n: number of elements), and with $\sum_i X_i = 1$,we yield n + w + 1 equations with the same number of unknowns (w unknown values X_i, n Lagrange-multipliers λ_i, and the sum $\sum_i m_i$). The calculation starts with a stoichiometric matrix whose elements are restricted by the mass balance condition and by the requirement of non-negativity, and it ends with the inversion of this matrix. The resulting values of the significant species are the basis for the new iteration cycle.

Phase diagrams can be constructed calculating the equilibrium composition for fixed temperatures and pressures. We have performed calculations for the Fe-O_2 system from 100K to 1900K in steps of 10K and for oxygen partial pressures from 10^{-23} mbar to 1 bar in steps of every full exponent. Whenever a change in the phase composition was observed, the temperature of the phase boundary line was further refined in steps of 1K. The Fe-H_2O phase diagram was determined analogously for temperatures ranging from 100K to 1300K and for water pressures from 10^{-11} mbar to 1 bar. Below room temperature, no thermodynamic data were provided by Equitherm and equilibrium compositions in this region are calculated by extrapolating the corresponding thermodynamic quantities to low temperatures. Compounds which are only stable below room temperature (e.g. water in its solid state) can not be included in the calculations.

2.2 Sample preparation

Iron oxide films were grown epitaxially onto Pt(111) single crystal substrates by repeated cycles of iron deposition and oxidation in oxygen pressures from 10^{-6} to 1 mbar at temperatures between 800 to 1200 K. Details about the preparation can be found elsewhere [6,19]. In some cases (as indicated), iron oxide films were grown on a Ru(0001) single crystal. Growth and formation of iron oxides on Ru(0001) has not yet been studied in such detail as on platinum substrates, nevertheless, the formation of the different iron oxide phases at various temperatures and oxygen pressures was verified by low-energy electron diffraction (LEED) and Auger electron spectroscopy (AES) to be identical to the growth on platinum. The Fe_2O_3 and Fe_3O_4 films prepared in this way are several few nanometers thick and exhibit the same properties as bulk single crystals as was shown by X-ray and ultra-violett photoelectron spectroscopy (XPS, UPS) and near-edge X-ray absorption spectroscopy (NEXAFS) measurements [20]. The surface and bulk structure of these surfaces was determined by scanning tunneling microscopy (STM), LEED, AES and transmission electron microscopy (TEM). STM, AES and LEED measurements were performed in a chamber with a base pressure of 1×10^{-10} mbar which is part of an ultra-high vacuum (UHV) system described in detail elsewhere [21]. The chamber is equipped with a STM (Burleigh), a backview LEED optics (Omicron) with video camera and digital image processing, an Auger electron spectrometer (Omicron), sample preparation facilities (Ar^+-sputter gun and iron evaporator), ion gauge and gas inlet systems. A transfer system allows to move the sample to and from a high pressure cell where preparation in high oxygen pressures up to 10 mbar at temperatures up to 1100 K are possible. Details about the specific structural investigations are published elsewhere [6,8,19,22-24]. Details on the conditions for the preparation of different phases are given in the context of section 4.3.

The temperature of the samples was measured via a nickel/nickel-chromium thermocouple which was spot-welded to the side of the platinum substrate. The actual temperature in most preparation procedures described below is probably higher than the measured temperature due to the limited thermal contact of the thermocouple and radiation losses. Measurements with a pyrometer indicated a tempera-

ture difference of up to 60K between the pyrometer measurement in the center of the sample and the thermocouple measurement on the edge of the Pt(111) single crystal. In the text we refer always to the temperature measured by a thermocouple. The pressure was measured by a commercially available Bayard-Alpert type ionization gauge (Granville-Phillips).

3. Crystal structures of iron oxides

Naturally occuring binary compounds of iron and oxygen include $Fe_{1-x}O$ (wustite), α-Fe_2O_3 (hematite), γ-Fe_2O_3 (maghemite) and Fe_3O_4 (magnetite). The ideal, stoichiometric FeO consists of Fe^{2+}-cations in all octahedral sites of a cubic close packed oxygen lattice (fig. 1a). The unit cell contains 4 formula units. This oxide occurs in a non-stoichiometric form $Fe_{1-x}O$, commonly known as wustite, with a deviation from stoichiometry x extending from 5% up to 15%. The iron deficiency is compensated by an oxidation of Fe^{2+}-ions to Fe^{3+}.

The oxygen atoms in magnetite (Fe_3O_4) form a close-packed face-centered cubic sublattice with Fe^{2+} cations located in octahedral sites and with Fe^{3+} cations equally distributed on octahedral and tetrahedral sites (inverse spinel structure). The cubic unit cell has a lattice constant of 8.396 Å and contains eight formula units and can be denoted as $(Fe_8^{3+})_{tetr}[Fe^{3+}Fe^{2+}]_8^{oct}O_{32}$ [7]. Along the (111) axis the oxygen layers are cubic close packed. Two types of iron sublayers occur inbetween them: A dense, so called Kagomé layer and a composite layer which consists of three mix-trigonal layers. Two of these mix-trigonal layers possess tetrahedrally coordinated Fe^{3+}, while the one inbetween them contains octahedrally coordinated Fe^{3+} (figure 1b). The Kagomé layer is characterized by laterally close packed hexagons and triangles forming a pattern where each side of the hexagon borders on a triangle, and each triangle is surrounded by three hexagons (fig. 1b). All iron cations in this layer are octahedrally coordinated, $^1/_3$ occur in the oxidation state Fe^{3+} and $^2/_3$ are in the formal valence +2.

Hematite (α-Fe_2O_3) crystallizes in the rhombohedral corundum structure. The hexagonal unit cell contains six formula units and exhibits lattice constants of a = 5.034 Å and c = 13.752 Å [25]. The oxygen anions form a hexagonal close packed sublattice with exclusively octahedrally coordinated Fe^{3+} species located in two thirds of the octahedral sites. Perpendicular to the (0001) direction the oxygen layers are hexagonal closed packed and alternate with two iron layers. Each of these is arranged in a mix-trigonal manner, both layers form a composite layer which is arranged in a honeycomb pattern (figure 1c).

Besides this modification there is one further naturally occuring binary oxide with a stoichiometry Fe_2O_3 namely maghemite (γ-Fe_2O_3), which exhibits a defect-spinel structure with a lattice constant of 8.35 Å very similar to the Fe_3O_4 structure. The Fe^{3+}-cations are arbitrarily distributed over octahedral and tetrahedral sites of the cubic closest packing of oxygen anions and it contains Fe^{2+} vacancies ($\otimes$) at octahedral sites resulting in a formula unit $(Fe^{3+})_8[Fe^{2+}_{5/3}\otimes_{1/3}]_8O_{32}$.

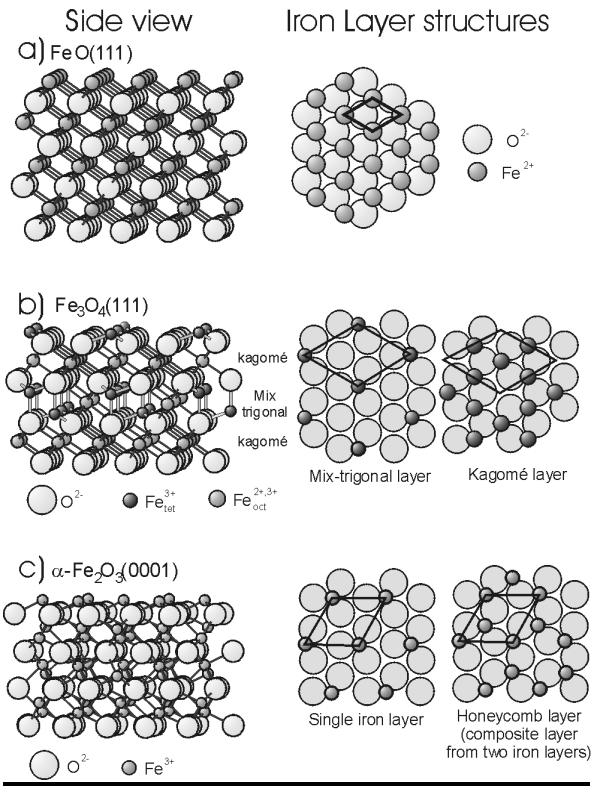

Fig. 1: a) Side view and top view of wustite FeO(111), assuming an iron termination. b) side view of magnetite Fe_3O_4(111), terminated by a mix-trigonal iron layer and top views for a termination by a mix-trigonal or a Kagomé-layer. These layers are arranged in a (2x2) periodicity with respect to the oxygen sublattice. c) Side view of hematite α-Fe_3O_4(0001), terminated by single iron layer and top views for the surface terminated by a single and a honeycomb layer. The iron layers form a $\sqrt{3}x\sqrt{3}R30°$ periodicity with respect to the oxygen sublattice.

4. Results and discussion

4.1 The system Fe-O_2

Phase diagrams are the most illustrative presentation of stability regions for different phases in dependence of variables like temperature and pressure. The coexistence of phases at equilibrium is commonly expressed by Gibbs' phase rule:

$$P + F = C + 2 \qquad (7)$$

with P: number of phases co-existing at equilibrium, F: number of degrees of freedom (in this case: temperature and oxygen pressure) and C: number of components determining all other species involved. A phase is defined as a physically distinguishable, defined and finite volume with a homogenous composition and strict boundaries. Because we have two components C in the iron-oxygen system, in each field of the phase diagram, where the oxygen pressure as well as the temperature is varied (F=2), only one phase can exist at equilibrium with the oxygen gas phase, while at the boundary curves (the boundary curves are determined by one degree of freedom since each temperature automatically determines the pressure and vice versa) two phases can coexist with the oxygen gas phase at equilibrium. For the calculations, we defined four solid phases for elemental iron, hematite, magnetite and wustite, for which we assumed no miscibility, one liquid phase containing iron, hematite, magnetite and wustite, and one oxygen gas phase. One mol solid iron and an excess of gaseous oxygen was preset. The resulting phase diagram shown in fig. 2 agrees very well with the one published by A. Muan [26].

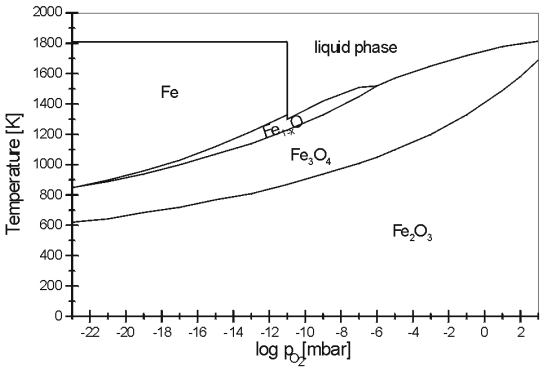

Fig. 2: Calculated temperature-pressure phase diagram for the iron-oxygen system.

The diagram shows that hematite is the stable phase at low temperatures. Beyond a boundary curve ranging from 640K at 10^{-23} mbar to 1690K at 1 bar magnetite is formed. In a field beyond this phase boundary and limited by a boundary curve ranging from 854K at $3x10^{-23}$ mbar to 1480K at 10^{-6} mbar, wustite becomes more stable. A special point in this phase diagram is the lowest temperature for which wustite remains a thermodynamically stable phase. Darken and Gurry reported 835K at 10^{-23} mbar [27] while inorganic textbooks often state 843K to be the lowest stability temperature for wustite [28]. Both values are slightly lower but agree reasonable with our calculated value (854K at $3x10^{-23}$ mbar). At even higher temperatures and below 10^{-11} mbar pure iron is formed. In oxygen pressures below 10^{-11} mbar, iron melts at 1804K. At 10^{-11} mbar, the melting temperature for a mixed iron-wustite solution drops to 1300K because of the lower melting point of pure wustite and due to freezing point depression for the mixed solution. With increasing pressure, the melting temperature rises to 1813K at 1 bar accompanied by an increasing amount of higher oxidized iron oxides in the liquid phase.

Table 1 shows the calculated free energies for $Fe_{1-x}O$, Fe_3O_4 and Fe_2O_3 at 1000K for five oxygen partial pressures for the reactions as shown in column 1. Since the oxygen gas molecules compete for the same amount of iron, all values are given in units of kJ per mol iron instead of the commonly used kJ/mol compound. These values give an impression of the relative stability of the different compounds. Especially for low pressures, the free energies are of the same order suggesting that all oxides may coexist in vacuum as metastable states because of kinetic hindering of the transition into the most stable states.

4.2 The system Fe-H_2O

In order to determine iron oxide stability regions in dependence of the water partial pressure, the different iron oxides, iron and water were included in the calculation as one liquid phase containing water, iron, hematite, wustite and magnetite, and as separate solid phases. Additionally we defined solid phases for goethite (α-FeOOH or $Fe_2O_3 \bullet H_2O$), bernalite ($Fe(OH)_3$) and $Fe(OH)_2$, and a gas phase containing water, molecular hydrogen and oxygen. First, an arbitrary excess of gaseous water (1000 mol) and 10 mol solid iron was preset. The calculated Fe-H_2O phase diagram in dependence of the water partial pressure and temperature is shown in figure 3a.

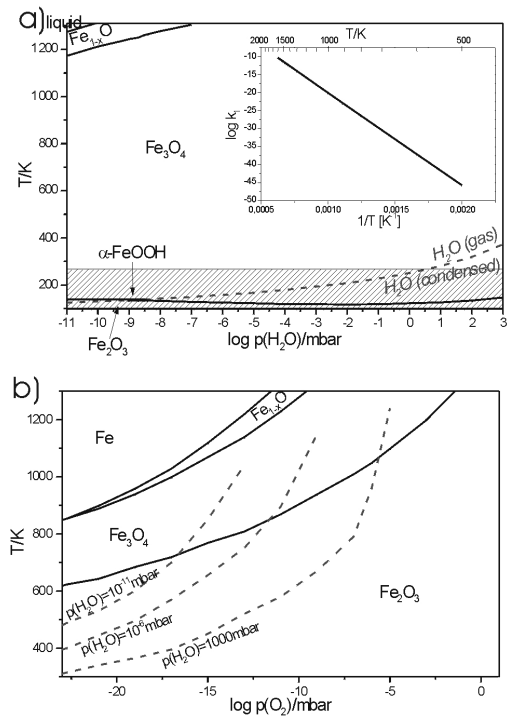

Fig. 3: a) Calculated temperature-pressure phase diagram for iron oxides and hydroxides. In the low-temperature region where water condenses, the pressure refers to the hydrogen pressure corresponding to the decomposition equilibrium of water. Below room temperature Equitherm extrapolates thermodynamic quantities of all phases which are stable above room temperature. Solid water (ice) is not considered. The inset shows a plot of the equilibrium constant k_1 vs. temperature (calculated from equation (16)). This phase diagram is *not* at thermodynamic equilibrium (see text). b) Calculated phase diagram in water atmosphere in dependence of the temperature and the oxygen pressure according to the decomposition equilibrium, equation (15). Dashed lines show H_2O isobars for 10^{-11}, 10^{-6} and 1000 mbar.

The phase boundary for the water condensation extends from 125K at 10^{-11} mbar to 373K at 1 bar. Below the respective condensation temperatures no water is present in the gas phase (it is not possible to consider vapor pressures of liquid phases in the equilibirum calculations) and the pressure is exclusively determined by the hydrogen partial pressure which is formed according to the equilibrium decomposition of water. The phase transition from magnetite to hematite occurs for temperatures below 150K for pressures between 10^{-11} and 1 bar. In a small region near the point of intersection of these two boundary curves, goethite (α-FeOOH) turns out as equilibrium phase. However, this result is not reliable since stability regions below room temperature are extrapolated on basis of the room temperature phases and a solid water phase is not included as mentioned in section 2.1. Very likely it would change the phase diagram below the melting point (gray shaded area). The phase diagram of water below the melting point is known to be very complicated due to the occurence of several crystalline and amorphous phases as well as supercooled water [29,30].

Table 1: Calculated free energies for different iron oxides and hydroxides at T=1000 K in dependence of the oxygen partial pressure (in kJ per turnover of one mol iron).

$p(O_2)$	10^{-10} mbar	10^{-6} mbar	10^{-3} mbar	1 mbar	1000 mbar
$Fe + \frac{1}{2}O_2 \rightarrow Fe_{1-x}O$	-71.3	-110.0	-139.1	-168.1	-197.2
$Fe + \frac{2}{3}O_2 \rightarrow \frac{1}{3}Fe_3O_4$	**-96.1**	-147.8	-186.5	-225.3	-264.0
$Fe + \frac{3}{4}O_2 \rightarrow \frac{1}{2}Fe_2O_3$	-91.5	**-149.6**	**-193.2**	**-236.8**	**-280.4**

Table 2: Relative stability of iron hydroxides with respect to hematite at 1 bar water pressure (in kJ/mol).

Chemical reaction	298 K	600 K	900 K
α-$Fe_2O_3 + H_2O \rightarrow \alpha$-FeOOH	+3.6	+35.9	+60.2
α-$Fe_2O_3 + 3H_2O \rightarrow 2Fe(OH)_3$	+60.8	+166.9	+293.6
α-$Fe_2O_3 + 4H_2O \rightarrow 2Fe(OH)_2 + 2H_2$	+808.7	+896.3	+1017.8

These results are relevant for the interpretation of structural investigations performed in ultra-high vacuum. The residual gas in UHV chambers is known to consist mainly of water, hydrogen and carbon monoxide, from which water is the most oxidizing compound. Therefore, this phase diagram may well represent the ambient atmosphere in residual gas atmospheres. In a residual gas pressure of 10^{-10} mbar a condensed phase of water will be formed below ~140K and may be present on the surface. This may explain ambiguities between structural investigations (e.g. by LEED crystallography) performed at 120K and theoretical structural determinations as reported for example for the Fe_3O_4(111) surface [31], as well as for the α-Al_2O_3(0001) surface structure [12,32]. The occurence of goethite near the water condensation line may indicate that surface hydroxyl groups may be formed at low temperatures in ultra-high vacuum.

To our surprise, the Fe_2O_3-Fe_3O_4 phase boundary turned out to shift toward lower temperatures when decreasing the H_2O:Fe ratio preset in the calculation. In contrast, the water condensation line and the high-temperature phase boundaries were not affected. The reason is that the available amount of oxygen for Fe oxidation is determined by the dissociation equilibrium of water $2H_2O \rightarrow 2H_2 + O_2$ with an equilibrium constant

$$k_1 = \frac{p_{O_2} p_{H_2}^2}{p_{H_2O}^2} \qquad (8)$$

Since dissociation is connected with an increase of the molar volume, pressure decrease favours dissociation. However, water dissociation is strongly endothermic. Although increasing with temperature, the partial pressure of O_2 remains very low for the temperature range considered here. This is demonstrated in the inset in fig. 3a which shows the temperature dependence of the equilibrium constant k_1. The iron is oxidized to Fe_3O_4 but for a given preset H_2O:Fe ratio, the available amount of oxygen may not be sufficient to oxidize all the iron further even if Fe_2O_3 would be the equilibrium phase. It turned our that a H_2O:Fe ratio of 10^{37}:1 is necessary to establish thermodynamic equilibrium at a pressure of 10^{-11}mbar and low temperature. For a sufficiently high H_2O:Fe ratio and beyond the condensation temperature, the partial pressure of water determines the oxygen partial pressure by means of equ. 8. This is illustrated by the water isobars included in fig. 3b which show the T-dependence of the oxygen partial pressure. The $p(H_2O)$-T phase diagram can therefore easily be transformed into a $p(O_2)$-T phase diagram. The latter is shown in fig. 3b. It turns out to be virtually identical to the phase diagram for the oxygen-iron system (fig. 2). No hydroxides appear to be stable in the considered p-T-range. The relative stability of the iron hydroxides with respect to hematite at 1 bar for different temperatures is shown in table 2. Whether water is included in the calculation or not, the composition of the iron oxides corresponds exactly to the oxygen partial pressure and beyond the condensation temperature, the presence of water or hydrogen has no influence on the phase composition. This has been used to determine Fe-O_2 phase diagrams for very low oxygen partial pressures. Instead of O_2, the decomposition equilibrium of H_2O or CO_2 was applied in order to establish very small O_2 partial pressures [25].

Depending on the pH [33], however, hydroxides may be stable in aqueous solution or in high water pressures. Thus, goethite becomes thermodynamically stable in the kbar regime [7,34]. Table 2 shows that goethite has a similar free energy than hematite at room temperature and for lower temperatures it may well become more stable since the phase diagrams shown in fig. 3 are only extrapolated below room temperature and the free energy changes associated with solid water are not considered.

4.3 Surface phases, transition structures and kinetic limitations

In the following we will compare the bulk thermodynamic phase diagram with the formation of thin iron oxide films in different oxygen pressures. Structural information gathered by LEED, STM, and Auger spectroscopy are summarized in figure 4. In general, the phase formation of thin iron oxide films at low oxygen pressures agrees well with the bulk stability regions but at the phase boundaries unique structures are observed.

Following the preparation procedure described above, first cycles of iron deposition and oxidation around 1000K in 10^{-6} mbar O_2 result in the growth of up to two layers of oxide with a stoichiometry and orientation corresponding to FeO(111) which completely wet the Pt(111) substrate [19,22]. This disagrees with the phase diagram (area A in figure 4) which suggests magnetite to be stable under these conditions. However, two monolayers with a stoichiometry of FeO represent not at all a thermodynamically formed bulk phase (the width of two monolayers FeO is even less than one unit cell of Fe_3O_4 (compare fig. 1)). The structure of one monolayer of FeO(111) on Pt(111) was determined

by photoelectron diffraction to be oxygen terminated and bound via an iron layer to the platinum substrate[35]. It turns out that the strong interaction of the first iron layer with the substrate stabilizes this oxide layer while the epitaxial relationship seems to play a minor role (the lattice mismatch is 12% and thus quite large). The same thin FeO layer was identified on Pt(100) by dynamical LEED investigations [36] and also on Ru(0001), we observe epitaxial growth of iron oxide films starting with FeO(111) (lattice mismatch 15%). It is striking that the first monolayers of heteroepitaxially grown iron oxide films on platinum, Ru(0001) or on other metals like Cu(001) [37] and on oxides as α-Al_2O_3(0001) [38] always grow with a stoichiometry and orientation of FeO(111), independent of preparation conditions and substrate. These monolayers completely wet the substrate and neutralize the influence of substrate and interface so that an oxidic layer of O^{2-} anions may serve as a kind of „nucleation ground“ for the iron oxide bulk phases expected from thermodynamics. Such a „buffer layer“ may provide the necessary stress release for the growth of the specific iron oxide phases.

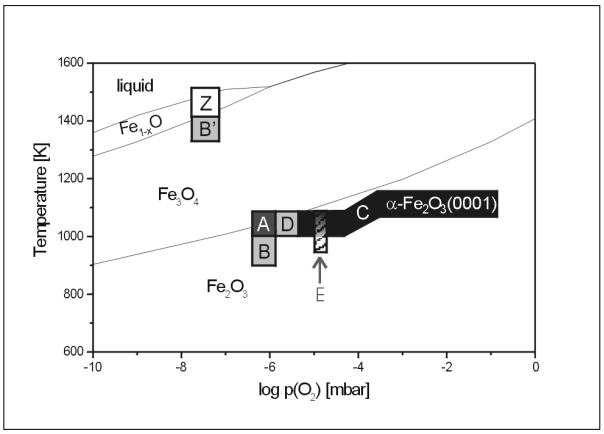

Fig. 4: Iron oxygen phase diagram from fig. 1 with regions where iron oxide surface phases were studied experimentally. The bottom of the boxes indicates the temperatures measured by a thermocouple spotwelded to the side of the sample. The actual temperature in the center of the sample is is estimated to be somewhere between the bottom and the top of the boxes (see section 2.2). (A): Preparation conditions for a regular, defect-free Fe_3O_4(111) surface. (B), (B'): Observation of biphase ordered Fe_3O_4(111) defect structures with FeO(111) domains. (C): Preparation conditions for α-Fe_2O_3(0001). (D) Intermediate surface structures consisting of long-range ordered FeO(111) domains coexisting with either magnetite or hematite depending on oxidizing (FeO(111)/Fe_3O_4(111)) or reducing (FeO(111)/α-Fe_2O_3(0001)) conditions. (E) New $\sqrt{3}x\sqrt{3}R30°$surface phase on α-Fe_2O_3(0001), coexisting with FeO(111) domains. (Z) Desorption of iron oxides.

We were not able to grow thick FeO films although we tried to prepare such films in a temperature and pressure range where the phase diagram predicts this phase to be stable (10^{-8}-10^{-7} mbar O_2, 1250-1470K, regions B', Z in fig. 4). Beyond ~1300K, the iron oxides start to desorb into the vacuum in a residual gas pressure of 10^{-10} mbar. In 10^{-8} mbar oxygen, the melting temperature for iron oxides should be higher and we observed the beginning of desorption beyond ~1350K (region Z in fig. 4). In the region denoted as B' in fig. 4, we observe a sharp LEED pattern from Fe_3O_4(111) intermixed with the main diffraction spots from FeO(111), suggesting that a partial reduction of magnetite occurs. Dieckmann and Schmalzried reported defect structures of magnetite which are characterized by cation deficiciencies near the phase boundary to hematite while near the phase boundary to wustite at high temperatures a cation excess is observed [39,40]. The dominant point defect in this case are iron interstitials, and we suppose that defective Fe_3O_4 in region B' disproportionates into iron-rich surface domains of FeO(111) and less defective Fe_3O_4. The corresponding rise in entropy may be compensated by the gain in lattice energy of the two phases at the surface where the lateral diffusion is facilitated. Prolonged heating always results in the desorption of the iron oxides until a very thin FeO(111) phase is left which desorbs at slightly higher temperatures. The LEED pattern and Auger spectra of this phase are almost identical to those obtained from 1-2ML FeO(111) in the initial growth stages so that we assume this phase to be of the same thickness. The thermal decomposition of the Fe_3O_4(111) proceeds via a FeO(111)-like surface phase. Longer treatment times should convert the whole film into FeO. However, the (111) surface of FeO is polar and should not be stable according to the autocompensation principle [41]. Therefore, it is energetically more favorable that the formed FeO desorbs immediately into the gas phase, so that the Fe_3O_4(111) film gets thinner until it disappears completely and only the FeO(111) termination with a thickness of 1-2ML remains on the substrate. To remove this, we have to increase the temperature in order to compensate for the substrate-FeO interaction. We do not observe the formation of a non polar termination as for example the FeO(100) phase which could be stable. Nevertheless, we cannot rule out that on cubic substrates thick non-polar FeO films may be formed in the predicted range of pressure and temperature.

Further cycles of iron deposition and oxidation result in islands of Fe_3O_4(111) which finally coalesce and form thick multilayer magnetite films [19]. From the phase diagram we would expect that magnetite forms beyond 1000K in 10^{-6} mbar oxygen partial pressure (field A in figure 4), while for lower temperatures (field B in figure 4) hematite should be stable. Fe_3O_4(111) films produced by annealing in 10^{-6} mbar oxygen at temperatures below 1000K exhibit defect structures with long-range ordered surface domains that are FeO(111) in nature (see fig. 5a), while temperatures beyond 1000K are necessary to obtain the regular Fe_3O_4(111) surface [23]. The superlattice formation was postulated to be due to the formation of FeO(111) islands which are limited in their lateral size due to the strain resulting from the lattice mismatch between the oxygen sublattices in FeO(111) (O-O distance: 3.04) and Fe_3O_4(111) (O-O distance: 2.90) [42]. At first glance, it seems not convincing that FeO domains are formed at lower temperatures since this would formally correspond to a partial reduction of the magnetite surface, whereas from the phase diagram we would expect an oxidation to hematite. However, we can explain this as follows: The Fe_3O_4(111) surface structure of all these films was determined by dynamical LEED calculations to be terminated by a mix-trigonal iron layer (see fig. 1) [23,24]. A recoordination of the tetrahedrally coordinated iron atoms to octahedral sites was suggested for the FeO(111) domains from STM measurements [23]. The adsorption of a monolayer of oxygen would correspond to the formation of FeO(111) domains, and if we define an oxidation as a process where oxygen atoms are incorporated into the crystal lattice of a solid these FeO domains are formed by an *oxidation* of the surface region. After several hours of tunneling, the STM measurements indicated adsorbates (presumably water) on the Fe_3O_4(111) domains while the FeO(111) domains remained adsorbate-free (see fig. 5a), indicating different chemical terminations for both domains. The oxidation state of surface atoms thus may strongly differ from the bulk oxidation state as has been shown by Mullikan population analyses for the V_2O_5(010) surface [43], and in addition, different surface terminations cause different oxidation states to exist over surface regions.

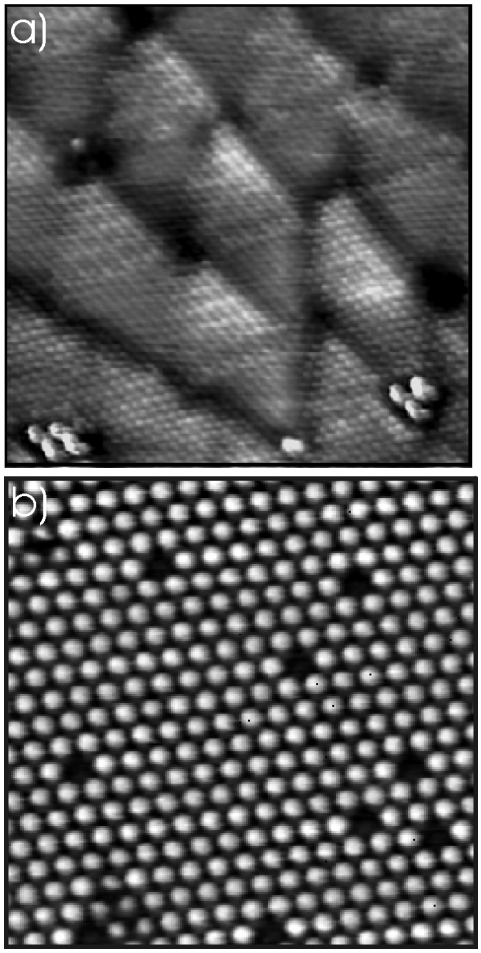

Fig. 5: Atomic resolution STM images of $Fe_3O_4(111)$ defect structures, U_t=+0.3V, I_t=1nA. a) 120x120 Å^2 image observed after preparation according to region (B) in fig. 4. Long range ordered FeO(111) domains in form of triangular patches are separated by regular $Fe_3O_4(111)$ areas (dark). The bright features in the lower part of the image are attributed to water contaminations and appear only on the $Fe_3O_4(111)$ termination [47]. b) 90x90Å^2 image observed after preparation according to region (A) in fig. 4. Bright protrusions form a 6x6Å unit cell and are attributed to Fe cations [23]. Statistically distributed Fe vacancies can be seen.

Another type of defects observed by STM on otherwise well-ordered $Fe_3O_4(111)$ films (region A in fig. 4) are statistically missing iron atoms (fig. 5b). From temperature-composition phase diagrams [44], it is known that the stability region of magnetite extends over a cation deficient region of non-stoichiometry. A corresponding cation deficient surface phase is obviously observed in the STM images. We can, however, not rule out that these defect structures on $Fe_3O_4(111)$ are no thermodynamic equilibrium structures. The free energy of magnetite at this pressure is only slightly higher than that of hematite (see table 1). Therefore defective metastable $Fe_3O_4(111)$ phases may be stabilized in this region of the phase diagram because of kinetically hindered oxygen incorporation.

In order to transform magnetite into hematite within a reasonable time (i.e. a few minutes), we found that oxygen partial pressures above 10^{-4} mbar and temperatures beyond 1000K were necessary (area C in fig. 4). For lower temperatures and oxygen pressures, the oxidation is slow, probably due to diffusion limitations: We have to offer higher oxygen pressures and lower temperatures than expected from the phase diagram to „push“ enough oxygen into the bulk (oversaturation). In order to transform magnetite into hematite in 10^{-4} mbar oxygen at 1000K, an oxidation time of about 30 minutes is necessary, and even in 10^{-5} mbar oxygen we finally observed the LEED pattern of α-$Fe_2O_3(0001)$ after long annealing times. A once prepared hematite surface phase may be reduced by decreasing the oxygen partial pressure below 10^{-6} mbar (at about 1000K) or by increasing the temperature. Density functional theory calculations predict two different terminations of hematite to be stable in high and low oxygen pressures [11]: In high oxygen pressures, a strongly relaxed oxygen terminated surface should form while in low oxygen pressures, a strongly relaxed iron terminated surface should be stable. STM images indeed reveal two different terminations to coexist on films annealed in 10^{-4} to 10^{-1} mbar oxygen [8]. In 1 mbar and in 10^{-5} mbar oxygen, respectively, single domains cover nearly 100% of the surface suggesting that the surface formed in 1 mbar oxygen corresponds to the oxygen-terminated structure found in the DFT calculations while the other one should be iron-terminated. The determination of these surface structures by dynamical Tensor-LEED investigations is not yet finished [45]: In 1 mbar oxygen a strongly relaxed oxygen terminated hematite surface could be identified while the analysis of the surface structure formed in 10^{-5} mbar is still subject to further investigations. The problems in the LEED analysis may be due to water contaminations since the I-V curves were recorded at 120K. Even at room temperature, slow contamination probably by H_2O was observed in STM [8]. An even faster contamination is expected at temperatures below the condensation temperature of water (fig. 3a). From theoretical calculations [11] the two surface terminations arise from equal surface energies at a specific oxygen gas phase chemical potential. Thus, no „phase width“ is expected from thermodynamic arguments. Therefore, we expect that the coexistence of two surface phases (mixed terminations) for a range of oxygen pressures between 10^{-1} and 10^{-4} mbar does not correspond to thermodynamic equilibrium but is a result of kinetic transport limitations. Further reduction of the oxygen pressure to 10^{-6} mbar oxygen (area D in figure 4) leads to a partial reduction of the hematite surface resulting in coexisting α-$Fe_2O_3(0001)$ and FeO(111) domains that are arranged in a biphase ordered superstructure similar to the one described in the literature [46].

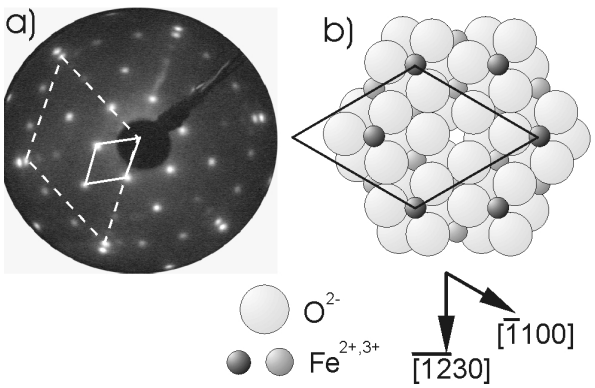

Fig. 6: a) LEED pattern (60eV) of an iron oxide phase prepared from Fe_2O_3 at T=1000K in 5x10^{-5} mbar O_2 (region E in fig. 4). The unit cells of the FeO(111)-(1x1) domains (dashed line) and of the $Fe_2O_3(0001)$-($\sqrt{3}$x$\sqrt{3}$)R30° structure (solid line) are indicated. b) Top view model of a possible arrangement for the $Fe_2O_3(0001)$-$\sqrt{3}$x$\sqrt{3}$R30° structure. Dark shaded iron atoms belong to the top iron layer (for details see text, compare also fig. 8).

Heating a magnetite film for 30 minutes in 5x10^{-5} mbar oxygen at 1000K (point E in figure 4) results in a new LEED pattern which is shown in fig. 6. This pattern exhibits a superposition of two diffraction patterns, one large reciprocal unit cell corresponding to FeO(111) with a periodicity of about 3.1 Å in real space, and another pattern

which exhibits a (√3x√3)R30° periodicity with respect to the α-Fe_2O_3(0001) pattern with a lattice constant of about 8 Å in real space. The orientation and lattice constant of the large reciprocal unit cell corresponds to the pattern reported for biphase ordered domains of FeO(111) on α-Fe_2O_3(0001) single crystals [46].

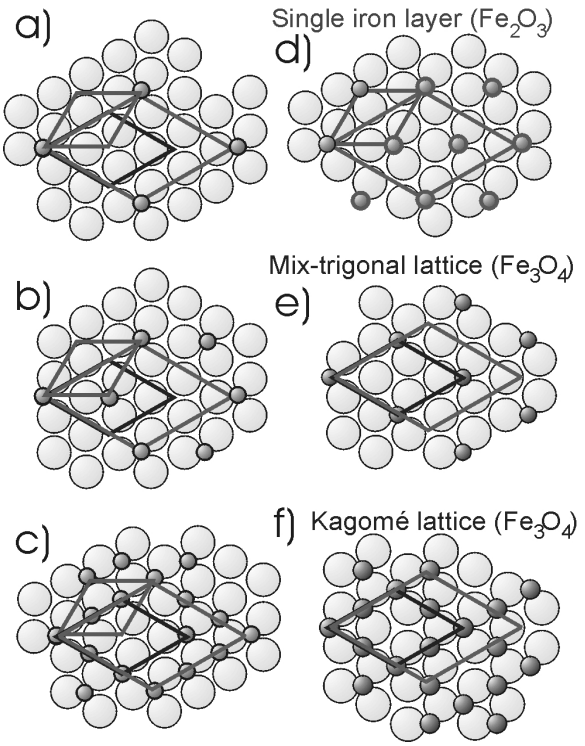

Fig. 7: a-c) Possible structure models for the iron sublayer in the observed Fe_2O_3(0001)-(√3x√3)R30° structure. d) Iron sublayer in α-Fe_2O_3(0001). e) One of the mix-trigonal layers and f) the Kagomé layer of Fe_3O_4(111). Compare also fig. 1.

Considering the iron sublattices in magnetite and hematite (see fig. 1), several structural models can be supposed for the new (√3x√3)R30° unit cell as shown in fig. 7: Models a) and b) are derived from the iron lattice in α-Fe_2O_3(0001) (fig. 7d) by removing $^2/_3$ or $^1/_3$ iron cations per unit cell, respectively. The model shown in figure 7c is derived from the Kagomé iron layer in Fe_3O_4(111) (fig. 7f). All these layers are iron deficient compared to the corresponding bulk layers. The iron deficiency may be compensated by the coexisting iron-rich FeO(111) domains. This would mean that magnetite disintegrates at the surface into FeO and an oxygen-rich phase under these conditions. As the valency of surface iron species is in unclear relation to the bulk valence states it cannot be excluded that the driving force for their disintegration is a valence change (disproportionation). Besides a surface reconstruction of the iron layers, we may think of a bulk transformation into a new iron oxide phase. Only one structural model for an oxidized bulk structure producing a (√3x√3)R30° pattern is compatible with electroneutrality. It can be constructed from the magnetite bulk structure by a lateral migration of iron cations in the three mix-trigonal layers into three layers of the type shown in fig. 7b, and the Kagomé layer should transform into one layer as shown in fig. 7c. The stoichiometry of one three-dimensional unit cell would be Fe_2O_3 and due to electroneutrality all iron cations in this structure should be Fe^{3+}. Such a bulk phase would correspond to an ordered variant of γ-Fe_2O_3(111), where the usually statistically distributed iron cations are periodically located in layers as shown in fig. 7b and c. All other structural models built up from the three layers shown in fig. 7a to c would either lead to iron oxidation states >+3 or to a splitting into more iron layers (assuming that the oxygen sublayers are still close packed). We found that this new √3x√3R30° structure is rather difficult to prepare, for identical preparation conditions the regular (1x1) pattern from α-Fe_2O_3(0001) or the √3x√3R30° pattern in combination with Fe_3O_4(111) or biphase ordered FeO(111) can be received. This suggests that this new structure is thermodynamically not stable but likely a metastable structure which is supported by the similarity to γ-Fe_2O_3 which is known to occur as a metastable intermediate in the oxidation of magnetite to hematite. Nevertheless, once prepared, this new structure turns out to be stable in ultra-high vacuum for at least a few days. Dynamical LEED and STM investigations are planned to clarify whether an extended γ-Fe_2O_3(111) phase is formed or whether a surface reconstruction of hematite produces the √3x√3R30° pattern.

Two different condensed phases can only coexist at thermodynamic equilibrium for a fixed temperature and pressure. This may be the case for the biphase ordered structures (areas B and D in fig. 4) which occur only in a narrow temperature and pressure range near the boundary curve between magnetite and hematite but according to the phase diagram we would then expect Fe_2O_3 to coexist with Fe_3O_4 instead of FeO on Fe_2O_3 or Fe_3O_4, respectively. These structures are thus metastable intermediates in the reduction as well as oxidation process. The occurence of FeO(111) surface domains in the investigated phase transformations among hematite and magnetite may be due to the fact that FeO(111) shows similarities to both the Fe_3O_4(111) structure and the α-Fe_2O_3(0001) structure. In all these structures, the oxygen anions form hexagonal sublayers. In wustite as well as in hematite all iron cations are octahedrally coordinated, while magnetite exhibits the same cubic close packing along the (111) axis as wustite. Therefore, the transformation of magnetite into wustite (and vice versa) requires mainly a recoordination of the iron cations which are very mobile in these two oxides, while the transformation of wustite to hematite (and vice versa) requires primarily a shift of the oxygen planes from a cubic close packed to a hexagonal close packed arrangement, which is facilitated by the predominant anionic diffusion of oxygen in hematite. The FeO(111) domains seem to nucleate on the iron oxides as a first step of the oxidation or reduction process before the bulk material starts to transform into the oxidized or reduced phases, respectively. We suggest the following general model for the growth and oxidation of iron oxides: First, a thin FeO(111)-like phase terminated by an oxygen layer is established. Into this sublattice, iron cations can be incorporated. Depending on the ambient temperature and oxygen partial pressure (i.e. the redox potential of the gas phase), different ratios of Fe^{3+} to Fe^{2+} are adjusted leading to the different iron oxide phases for the conditions represented by the phase diagram (fig. 2). The incorporation of iron cations may initially be statistical leading to defect structures as observed for Fe_3O_4 below 1000K, but becomes ordered by annealing at higher temperatures.

The observed equilibrium surface phases (areas A and C in fig. 4) are summarized in table 3. Structures observed in areas B, B', D and E are presumably intermediate surface structures forming in the oxidation or reduction of magnetite or hematite, respectively. All intermediate and equilibrium iron oxide structures discussed are metastable at room temperature for long periods which is simply due to the slow kinetics at room temperature.

Table 3: Structures and stability regions of equilibrium iron oxide surface phases. For details see text.

Preparation condition	Surface structure
>1000K, $<10^{-6}$ mbar O_2	Fe_{tet}^{3+}-terminated $Fe_3O_4(111)$, unreconstructed, strongly relaxed
~1000K, 10^{-5} mbar O_2	α-$Fe_2O_3(0001)$, unreconstructed (under investigation)
~1100K, 1 mbar O_2	O-terminated α-$Fe_2O_3(0001)$, unreconstructed, relaxed

5. Conclusions

Phase diagrams for the system iron-oxygen in dependence of the temperature and oxygen partial pressure have been calculated. We found that the formation of thin, epitaxial iron oxide films agrees very well with the predicted bulk stability regions. Up to 1 bar, water has no thermodynamic influence on the composition of iron oxides although water strongly affects the kinetics of redox processes of iron oxides [48,49]. In its gaseous state, water acts as an oxidizing compound and the oxygen partial pressure corresponding to the decomposition equilibrium of water into hydrogen and oxygen determines the stability of the iron oxides just as the pure oxygen partial pressure does. Surface science experiments in ultra-high vacuum at temperatures below ~140K have to be evaluated with great care since a thin film of water may have condensed on the surface.

We always observe the formation of ordered FeO(111) domains in the initial stages of the growth of iron oxides as well as in a temperature and pressure range near the Fe_2O_3-Fe_3O_4 phase boundary where the transformation of the iron oxide bulk phases appears to be kinetically hindered. We presume that these domains formed on $Fe_3O_4(111)$ under oxidizing and on α-$Fe_2O_3(0001)$ under reducing conditions actually represent an oxidized or reduced intermediate surface phase which always forms as a first „nucleation“ step in the oxidation of magnetite as well as in the reduction of hematite, respectively. Depending on the ambient temperature and oxygen pressure, different Fe^{3+} to Fe^{2+} ratios are incorporated into this oxygen-rich surface sublattice leading to the different iron oxide phases. The oxidation of $Fe_3O_4(111)$ to α-$Fe_2O_3(0001)$ was furthermore found to proceed via a new intermediate surface phase which we could observe after annealing in $5x10^{-5}$ mbar O_2 at 900-1000K probably consisting of an iron-deficient Fe_2O_3 region with similarities to γ-$Fe_2O_3(111)$. For surface processes, including catalysis, all discussed surface phases are of dominating interest.

We have demonstrated that thermodynamics in combination with surface science experiments may well serve as a tool for the determination of equilibrium and intermediate surface structures of compound materials in dependence of the temperature and ambient gas phase pressure. Thin, epitaxially grown compound films are ideal model systems to elucidate the relevance of surface phases in chemical transformations, since the amount of the compound is limited and hence kinetic limitations due to diffusion processes are minimized.

Acknowledgements:

The authors thank Christian Kuhrs and Yvonne Joseph from the Fritz-Haber Institut for experimental support and Sh. K. Shaikhutdinov from the Fritz-Haber Institut for the STM images.

References

[1] E. H. Lee, *Catal. Rev.*, 1973, **8**, 285.
[2] M. Muhler, R. Schlögl, and G.Ertl, *J. Catal.*, 1992, **138**, 413.
[3] C. Kuhrs, Y. Arita, W. Weiss, W. Ranke, and R. Schlögl, submitted to *Top. in Catal*.
[4] S. C. Street, C. Xu, and D. W. Goodman, *Annu. Rev. Phys. Chem.*, 1997, **48**, 43.
[5] W. Weiss, and R. Schlögl, *Top. in Catal.*, 2000, **13**, 75.
[6] Sh. K. Shaikhutdinov, Y. Joseph, C. Kuhrs, W. Ranke, and W. Weiss, *Faraday Discuss.*, 1999, **114**, 363.
[7] *The Iron Oxides,* ed. R. M. Cornell, and U. Schwertmann, VCH Weinheim, 1996.
[8] Sh. K. Shaikhutdinov, and W. Weiss, *Surf. Sci. Lett.*, 1999, **432**, L627.
[9] P. Liu, T. Kendelewicz, G. E. Brown, Jr., E. J. Nelson, and S. A. Chambers, *Surf. Sci.*, 1998, **417**, 53.
[10] P. Liu, T. Kendelewicz, G. E. Brown, Jr., and G. A. Parks, *Surf. Sci.*, 1998, **412/413**,287.
[11] X.-G. Wang, W. Weiss, Sh. K. Shaikhutdinov, M. Ritter, M. Petersen, F. Wagner, R. Schlögl, and M. Scheffler, *Phys. Rev. Lett.*, 1998, **81**, 1038.
[12] X.-G. Wang, A. Chaka, and M. Scheffler, *Phys. Rev. Lett.*, 2000, **84**, 3650.
[13] e.g.: J. Kucera, and M. Hajduga, *Oxid. Met.*, 1994, **41**, 1.
[14] e.g.: S. J. Roosendaal, A. M. Vredenberg, and F. H. P. M. Habraken, *Surf. Rev. Lett.*, 1999, **6**, 1229.
[15] V. Stambouli, C. Palacio, H. J. Mathieu, and D. Landolt, *Appl. Surf. Sci.*, 1992, **70/71**, 240.
[16] R.J. Lad, and V. E. Henrich, *Surf. Sci.*, 1988, **193**, 81.
[17] Equitherm, *„Database and software package for chemical equilibrium calculations on personal computers.“*, Version 3.02, VCH Scientific software, 1993.
[18] I. Barin, *Thermochemical Data of Pure Substances*, VCH Weinheim, 2nd Edition, 1992.
[19] W. Weiss, and M. Ritter, *Phys. Rev.*, 1999, **B59**, 5201.
[20] T. Schedel-Niedrig, W. Weiss, and R. Schlögl, *Phys. Rev.*, 1995, **B52**, 17449.
[21] W. Weiss, M. Ritter, D. Zscherpel, M. Swoboda, and R. Schlögl, *J. Vac. Sci. Technol.*, 1998, **A16**,21.
[22] W. Ranke, M. Ritter, and W. Weiss, *Phys. Rev.*, 1999, **B60**, 1527.
[23] Sh. K. Shaikhutdinov, M. Ritter, X.-G. Wang, H. Over, and W. Weiss, *Phys. Rev.*, 1999, **B60**, 11062.
[24] M. Ritter, and W. Weiss, *Surf. Sci.*, 1999, **432**, 81.
[25] R. W. G. Wyckhoff, *Crystal Structures,* 2nd Ed., Vol. I-III, Interscience Publishers, 1982.
[26] A. Muan, *Am. J. Sci*., 1958, **256**, 176.
[27] L.S. Darken, and W. Gurry, *J. Am. Chem. Soc.*, 1945, **67**, 1398.
[28] e.g.: A. F: Holleman, and N. Wiberg, *Lehrbuch der Anorganischen Chemie*, 91.-100. Auflage, de Gruyter Berlin, New York, 1985.
[29] *Water - A comprehensive treatise, Vol. 1: The Physics and Physical Chemistry of Water*, Ed. Felix Franks, Plenum Press New York-London, 1972.

[30] H. E. Stanley, S. V. Buldyrev, M. Canpolat, O. Mishima, M. R. Sadr-Lahijany, A. Scala, and F. W. Starr, *PCCP*, 2000, **2**, 1551.
[31] J. Ahdjoudj, C. Martinsky, C. Minot, M. A. Van Hove, and G. A. Somorjai, *Surf. Sci.*, 1999, **443**, 133.
[32] J. Toofan, and P. R. Watson, *Surf. Sci.*, 1998, **401**, 162.
[33] H. H. Le, and E. Ghali, *J. Appl. Electrochem*., 1993, **23**, 72.
[34] I. Diakanov, I. Khodakovsky, J. Schott, and E. Sergeev, *Eur. J. Min.*, 1994, **6**, 967.
[35] Y. J. Kim, C. Westphal, R. X. Ynzunza, H. C. Galloway, M. Salmeron, M. A. Van Hove, and C. S. Fadley, *Phys. Rev.*, 1997, **B55**, R13448.
[36] M. Ritter, H. Over, W. Weiss, *Surf. Sci.*, 1997, **371**, 245.
[37] J. Karunamuni, R. L. Kurtz, and R. L. Stockbauer, *Surf. Sci.*, 1999, **223**, 223.
[38] S. Gota, E. Guiot, M. Henriot, and M. Gautier-Soyer, *Phys. Rev.*, 1999, **B60**, 14387.
[39] R. Dieckmann, *Ber. Bunsenges. Phys. Chem.,* 1982, **86**, 112.
[40] R. Dieckmann, H. Schmalzried, *Ber. Bunsenges. Phys. Chem.*, 1977, **81**, 414.
[41] P. W. Tasker, *J. Phys. C*, 1979, **12**, 4977.
[42] N. G: Condon, F. M. Leibsle, T. Parker, A. R. Lennie, D. J. Vaughan, and G. Thornton, *Phys. Rev. B*, 1997, **B55**, 15885.
[43] K. Hermann, M. Witko, and R. Druzinic, *Faraday Discuss.*, 1999, **114**, 53.
[44] H. Schmalzried, *Solid State Reactions*, VCH Weinheim, Acad. Press 1974, p. 196.
[45] G. Ketteler, W. Weiss, and W. Ranke, in preparation.
[46] N. G. Condon, F. M. Leibsle, A. R. Lennie, P. W. Murray, T. M. Parker, D. J. Vaughan, and G. Thornton, *Phys. Rev. Lett.*, 1995, **75**, 1961.
[47] Sh. K. Shaikhutdinov, W. Weiss, *J. Molec. Catal. A: Chemical*, 2000, **158**, 129.
[48] R. Schlögl, „*Preparation and Activation of Technical Ammonia Synthesis Catalyst.“* In: *Catalytic Ammonia Synthesis, Fundamental and Practice*, Ed. R. J.
Jennings. Plenum, 1991, 19-107.
[49] A. Baranski, A. Kotarba, J. M. Lagan, A. Pattek-Janczyk, E. Pyrczak, and A. Reizer, *Appl. Catal. A: General*, 1994, **112**, 13.